Title

Congenital Zika virus infection as a silent pathology with loss of neurogenic output in the fetal brain

Permalink

https://escholarship.org/uc/item/27j088xp

Journal

Nature Medicine, 24(3)

ISSN

1078-8956

Authors

Adams Waldorf, Kristina M
Nelson, Branden R
Stencel-Baerenwald, Jennifer E
et al.

Publication Date

2018-03-01

DOI

10.1038/nm.4485

Peer reviewed

Congenital Zika Virus Infection as a Silent Pathology With Loss of Neurogenic Output in the Fetal Brain

Kristina M. Adams Waldorf[1,2,3,4,#], **Branden R. Nelson**[5,*], **Jennifer E. Stencel-Baerenwald**[2,6,*], **Colin Studholme**[7,8,9,*], **Raj P. Kapur**[10,11,*], **Blair Armistead**[3,12,*], **Christie L. Walker**[1,*], **Sean Merillat**[12,*], **Jay Vornhagen**[3,12,*], **Jennifer Tisoncik-Go**[2,6,*], **Audrey Baldessari**[13], **Michelle Coleman**[7,12], **Manjiri K. Dighe**[9], **Dennis W.W. Shaw**[9,14], **Justin A. Roby**[2,6], **Veronica Santana-Ufret**[12], **Erica Boldenow**[7,12], **Junwei Li**[8], **Xiaohu Gao**[8], **Michael A. Davis**[2,6], **Jesica A. Swanstrom**[15], **Kara Jensen**[15], **Douglas G. Widman**[15], **Ralph S. Baric**[15,16], **Joseph T. Medwid**[17], **Kathryn A. Hanley**[17], **Jason Ogle**[13], **G. Michael Gough**[13], **Wonsok Lee**[13], **Chris English**[13], **W. McIntyre Durning**[13], **Jeff Thiel**[9], **Chris Gatenby**[9], **Elyse C. Dewey**[2,6], **Marian R. Fairgrieve**[2,6], **Rebecca D. Hodge**[18], **Richard F. Grant**[13], **LaRene Kuller**[13], **William B. Dobyns**[5,7], **Robert F. Hevner**[5], **Michael Gale Jr.**[2,3,6,#], and **Lakshmi Rajagopal**[2,3,7,12,#]

[1]Department of Obstetrics & Gynecology, University of Washington, Seattle, Washington, United States of America

[2]Center for Innate Immunity and Immune Disease, University of Washington, Seattle, Washington, United States of America

[3]Department of Global Health, University of Washington, Seattle, Washington, United States of America

[4]Sahlgrenska Academy, Gothenburg University, Sweden

[5]Center for Integrative Brain Research, Seattle Children's Research Institute, Seattle, Washington, United States of America

[6]Department of Immunology, University of Washington, Seattle, Washington, United States of America

[#]Address correspondence to Kristina Adams Waldorf (adamsk@uw.edu), Michael Gale, Jr. (mgale@uw.edu) and Lakshmi Rajagopal (lakshmi.rajagopal@seattlechildrens.org).
[*]Equal Contribution

[7]Department of Pediatrics, University of Washington, Seattle, Washington, United States of America

[8]Department of Bioengineering, University of Washington, Seattle, Washington, United States of America

[9]Department of Radiology, University of Washington, Seattle, Washington, United States of America

[10]Department of Pathology, University of Washington, Seattle, Washington, United States of America

[11]Department of Pathology, Seattle Children's Hospital, Seattle, Washington, United States of America

[12]Center for Global Infectious Disease Research, Seattle Children's Research Institute, Seattle, Washington, United States of America

[13]Washington National Primate Research Center, Seattle, Washington, United States of America

[14]Department of Radiology, Seattle Children's Hospital, Seattle, Washington, United States of America

[15]Department of Epidemiology, University of North Carolina at Chapel Hill, Chapel Hill, North Carolina, United States of America

[16]Department of Microbiology and Immunology, University of North Carolina at Chapel Hill, Chapel Hill, North Carolina, United States of America

[17]Department of Biology, New Mexico State University, Las Cruces, New Mexico, United States of America

[18]Allen Institute for Brain Science, Seattle, WA

Abstract

Zika virus (ZIKV) is a flavivirus with teratogenic effects on the fetal brain, but the spectrum of brain injury is unknown, particularly when ultrasound imaging is normal. In a pregnant pigtail macaque (*Macaca nemestrina*) model, we demonstrate that ZIKV injury to the fetal brain was significant even in the absence of microcephaly and is clinically challenging to detect. A common and subtle injury pattern was identified including: 1) periventricular T2-hyperintense foci and loss of fetal non-cortical brain volume, 2) injury to the ependymal epithelium with underlying gliosis, and 3) loss of late fetal neuronal progenitor cells in the subventricular zone (temporal cortex) and subgranular zone (dentate gyrus, hippocampus) with dysmorphic granule neuron patterning. Attenuation of fetal neurogenic output demonstrates potentially significant teratogenic effects of congenital ZIKV infection even without microcephaly. All children exposed to ZIKV in utero should be followed long-term for neurocognitive deficits, regardless of head size at birth.

Introduction

A recent epidemic of Zika virus (ZIKV) in the Americas became a global public health emergency after an unexpected surge in prenatal and congenital microcephaly suggested that

the virus was teratogenic in pregnancy. ZIKV is a Flavivirus transmitted by the bite of *Aedes* mosquitoes. ZIKV is neurotropic and can target neural progenitor cells, astrocytes and neurons in all stages of development.[1] Infection typically induces an asymptomatic or mild infection characterized by fever, rash, and arthralgia. The congenital ZIKV syndrome describes a severe pattern of fetal brain injury including microcephaly and ocular injury associated with infection during pregnancy.[2] Counseling pregnant women with ZIKV infection is limited by a lack of understanding of the spectrum and prevalence of fetal injury. [3] While the association between ZIKV and microcephaly is known, recent reports have supported a broad spectrum of injury in infants with a normal head circumference at birth including eye abnormalities and development of postnatal microcephaly[4–8]. There is an urgent need for development of a pathophysiologically relevant animal model to support pre-clinical characterization of vaccines[9–14] and therapeutics.[15,16] We previously reported fetal brain injury in a pregnant pigtail macaque (Macaca *nemestrina*) subcutaneously infected with ZIKV.[17] Here, we describe an expanded series of ZIKV infections in pregnant pigtail macaques, including the prior case report[17], wherein significant loss of fetal neuronal progenitor cells accompanied a characteristic pattern of brain injury.

Results

Clinical Course of ZIKV infection in Pregnant Nonhuman Primates

We inoculated ZIKV subcutaneously at five separate locations on the forearms (total inoculum 5×10^7 plaque-forming units) into five healthy pregnant pigtail macaques, identified as ZIKA 1, 2, 3, 4, and 5 (Fig. S1, Table S1). A Cambodian ZIKV strain (F2213025, 2010) was inoculated at 119 (ZIKA 1[17]) and 82 (ZIKA 2) days gestation. For ZIKA 3–5, a Brazilian ZIKV strain (Fortaleza, 2015) was inoculated with *Aedes egypti* salivary gland extract (SGE, ~4 glands/inoculum, shown to enhance flavivirus infection)[18,19] at 60–63 days gestation. ZIKA 3–5 also received a monoclonal dengue virus antibody (DENV-Ab; EDE2 B7, 1 mg intravenous)[20] prior to viral inoculation and three weeks later to model antibody-dependent enhancement, thought to occur in some human cases due to DENV-Ab (Fig. S2).[21,22] Control animals received media inoculation with mosquito SGE and EDE2 B7 antibody (CTRL 2) or with media alone (CTRL 1, 3). Prior to inoculation, all animals were seronegative for ZIKV and related Flaviviruses (Table S2). Animals were delivered by Cesarean section in the absence of labor within one month of their due date to enable collection of placental and fetal tissues before birth (~172 days gestation).

Three of five animals appeared healthy without evidence of fever, conjunctivitis or obstetrical complications of pregnancy (e.g. preterm labor). Seven days after inoculation, ZIKA 3 developed intermittent rectal bleeding. In ZIKA 5, a rash developed on the forearms two days after inoculation and resolved after six days (Fig. S3). ZIKV IgG became detectable in maternal sera of all ZIKA animals between days 10–18 after inoculation and in the amniotic fluid from 4 of 5 ZIKA fetuses (Table S2). ZIKV RNA was detected in maternal sera of ZIKA animals only on day 2 and not in controls (Fig. S4A). ZIKV RNA was also detected in the brain and other organs from dams and fetuses of ZIKA 1 and 2, but not in controls or ZIKA animals with a longer latency between inoculation and delivery

(Table S3). ZIKV infectious isolates were recovered from maternal plasma of two animals with the highest viral load (ZIKA 4 and 5, Fig. S4B).

Fetal Brain Lesions by MRI

No obvious fetal abnormalities were detected by weekly ultrasound with the exception of a periventricular echogenic lesion and ventriculomegaly in ZIKA 1, as previously described.[17] Over time, maternal ZIKV infection was associated with a growth deceleration in the fetal biparietal diameter and abdominal circumference, particularly in late gestation, which did not meet criteria for microcephaly (biparietal diameter <2 SD below the mean; Fig. S5). Doppler assessment of the fetal middle cerebral artery revealed no differences in the resistance index suggesting that fetal brain oxygenation was similar between groups (mean 0.7, both groups). Fetal brain MRI images were abnormal in 4 of 5 animals using a HASTE (half-Fourier acquisition single-shot turbo spin-echo, T2-weighted) pulse sequence (Fig. S1). Periventricular-subcortical T2-hyperintense foci developed in the posterior brain in ZIKA 1, 2, 3, and 5 between 120–129 days and were absent in controls (Fig. 1A, Fig. S6–S11). The brainstem and cerebellum appeared normal with the exception of a posterior fossa arachnoid cyst in ZIKA 1 (Fig. S12). We controlled for natural variations in fetal brain size by analyzing the proportion that non-cortical tissues (excluding cortical plate) contributed to overall fetal brain volume (Fig. 1B, S13). The ratio of non-cortical tissues to total brain volume was similar among cases and controls until ~100 days, when the relative proportion of non-cortical tissues to overall brain volume began to diverge leading to a significantly smaller ratio in ZIKA fetuses at delivery (p=0.01, Fig. 1B).

Pathologic Changes in the Brain and Placenta

We previously described neuropathology in ZIKA 1, which demonstrated ependymal loss, fusion of ventricular surfaces, periventricular gliosis, white matter gliosis and axonal spheroids (axonal injury).[17] A consistent pattern of neuropathology was identified in ZIKA 2, 3 and 4, which showed a spectrum of severity for these features and was absent in controls; the most consistent finding was ependymal injury in the posterior lateral ventricles. Ependymal loss, interruption of the lumen, fusion of denuded ventricular surfaces, and/or GFAP-immunoreactive gliosis in the white matter beneath the ventricle surface was most prominent in ZIKA 1 and 2 with similar, but milder changes in ZIKA 3 and 4 (Fig. 2; Table S4). There was no significant neuropathology in ZIKA 5; interestingly, and in contrast to the other ZIKA animals, NK cell populations in the placenta and maternal blood for ZIKA 5 were similar to controls (Fig. S14). No distinct pathologic abnormalities were seen in other fetal or maternal organs with the exception of minimal maternal myocardial fibrosis in ZIKA 4. Placental histopathology revealed only mild deciduitis, which was also present in some controls (Fig. S15).

Loss of Neural Stem Cells in Late Fetal Neurogenic Zones

ZIKV infects and kills neural stem cells (NSCs) including early neuroepithelial progenitors, radial glia and intermediate progenitor cells (IPs).[23,24] As we ended the study near the natural due date, we hypothesized that remaining "late" neurogenic populations in the subventricular zone (SVZ) of the temporal cortex and the subgranular zone (SGZ) of the dentate gyrus (DG) in the fetal hippocampus were affected by congenital ZIKV exposure

(Fig. 3A–C).[25–28] Although SVZ and SGZ NSCs are actively neurogenic and express similar markers, each generates different types of neurons[29] and may be differentially affected by ZIKV[30] due to lateral ventricle proximity, differences in regional vasculature, and sensitivity to inflammatory signals. We examined sections by immunolabeling for the proliferative marker Ki67 (Fig. 3D–G), and found a significant reduction in Ki67+ cells in ZIKA fetuses versus controls in the SVZ compared to SGZ (p=0.03, Fig. 3H and S16). We also immunolabeled adjacent sections for Sox2 and Tbr2 proteins (Fig. 4A–C, S16), which mark quiescent/active NSCs and IPs, respectively.[31,32] Congenital ZIKV exposure was associated with a trend towards reduction in fetal Sox2+ cells in the SVZ (p=0.06, Fig. 4D); in the SGZ niche, Sox2+ NSC appeared disorganized. Tbr2+ IPs in ZIKA fetuses were significantly reduced in the SGZ (p=0.006, Fig. 4E–H, S17). Moreover, Sox2/Tbr2/Dcx triple-immunolabeling of adjacent sections revealed that Sox2+ NSC disorganization and loss of Tbr2+ IPs in the SGZ niche was accompanied by dysmorphia in the Dcx+ (doublecortin) maturing granule neuron (GN) neural circuitry (Fig. 4F–H, S18). Flow cytometry analysis of cells isolated from cortical white matter tracts also revealed a significant increase in astrocytes with congenital ZIKV exposure indicating a gliotic response to nervous system injury (p=0.02, Fig. S19).

Discussion

An enduring obstetric challenge of the ZIKV epidemic is the antenatal identification of the spectrum of ZIKV-associated fetal brain injury not captured by the definition of the congenital ZIKV syndrome. Our study reveals that ZIKV exposure can cause a spectrum of subtle fetal brain injuries in the absence of overt microcephaly, including loss of late fetal NSCs in sites that normally persist into adult life, perturbations to neuron patterning, and astrocyte gliosis. Within a highly relevant maternal-fetal transmission model of ZIKV infection, we identified a characteristic profile of fetal brain injury that is exceedingly difficult to detect clinically, even with the aid of serial ultrasound and MRI. A deceleration in growth of the biparietal diameter and abdominal circumference may not be considered clinically abnormal, especially if the fetus is constitutionally large or ZIKV infection occurs late in gestation. T2-hyperintense foci were detected by MRI, but only transiently, and this imaging modality is not widely available. Our study highlights the inability of standard prenatal diagnostic tools to detect silent pathology in the fetal brain associated with congenital ZIKV infection in the absence of microcephaly.

Our novel finding that ZIKV attenuates late fetal neurogenesis is concerning for the long-term effects on fetuses that did not meet criteria for microcephaly at birth. Neurogenesis normally persists in the human hippocampus through at least adolescence[33] and is important for learning[29] and memory[29]. Attenuation of these NSC and IP populations may predispose not only to microcephaly, but also to the long-term development of Alzheimer's disease[34], schizophrenia[35], and depression[36]. The loss of adult NSCs due to ZIKV infection has been reported in a highly immunocompromised non-pregnant mouse (lacking interferon regulatory factor (IRF)3, IRF5, and IRF7).[37] Our findings now confirm that late NSC populations are impacted in the fetus of an immunocompetent and pathophysiologically relevant nonhuman primate model. If altered neurogenesis occurs in human children and adolescents infected with ZIKV post-birth, similar to our findings in fetal nonhuman

primates, a risk for the early onset of neurocognitive and psychiatric conditions could extend beyond infection in utero. It is also possible that quiescent NSCs may become activated to repair neural circuitry following less severe ZIKV-induced injury.

The strength of our study lies in the first *in vivo* molecular characterization of the effects of maternal ZIKV infection on the fetal brain demonstrating: 1) deficient fetal neuronal progenitor cell populations concomitant with non-cortical volume loss of the fetal brain, 2) perturbations in neuron maturation and patterning in the hippocampus, and 3) increased astrocyte gliosis. Less white matter gliosis in ZIKA 3, 4 and 5 (inoculation ~60 days) compared to ZIKA 1 and 2 (inoculation 82–119 days) may reflect the limited capacity for a gliotic response of the early fetal brain rather than differences in viral strain or lack of potentiation by *Ae. aegypti* salivary gland proteins or antibody-dependent enhancement.[38] The sample size precludes drawing conclusions as to slight variations in study design, which reflected attempts to observe a more severe phenotype with inoculation earlier in pregnancy coupled with a Brazilian ZIKV strain and DENV-Ab with antibody-dependent enhancement properties.[20] Despite variations in study design (e.g. viral strain), the effect of maternal ZIKV infection on NSC loss was fairly consistent in all ZIKV animals; notably, inoculation of SGE and DENV-Ab alone was not associated with fetal brain injury in CTRL 2. Although antibody dependent enhancement was not demonstrated in a study of non-pregnant nonhuman primates[39], this question should be evaluated in pregnancy and the developing fetus. A recent study associating DENV-Ab titer with severe dengue disease in a large pediatric cohort provides important evidence for enhancement associated with antibody titer, which is challenging to model experimentally.[40]

Our findings underscore the formidable obstetric challenge of diagnosing ZIKV-associated fetal brain injury, as a loss in fetal brain volume may be subtle, and normal ultrasound imaging of the fetal brain does not correlate with the absence of fetal brain injury. Attenuation and/or loss of NSCs not only elevates concern for long-term effects of congenital ZIKV exposure for neonates regardless of head size at birth, but also for children and young adults that acquire ZIKV post-birth. Additional research is needed to determine whether ZIKV infection in utero or childhood is associated with an elevated risk for neurocognitive and psychiatric disorders.

Online Methods

Study Design

The nonhuman primate experiments were carried out in strict accordance with the recommendations in the Guide for the Care and Use of Laboratory Animals of the National Research Council and the Weatherall report, "The use of non-human primates in research". The Institutional Animal Care and Use Committee (IACUC) of the University of Washington (UW) approved the study (Permit Number: 4165-02). Cesarean section was performed at least 10 days before the natural due date (~172 days) to enable fetal and dam necropsy. We based the ZIKV inoculum dose on the feeding behavior of the ZIKV mosquito vector, *Aedes aegypti* (yellow fever mosquito), which deposits virus multiple times during skin probing prior to accessing a capillary for acquisition of the bloodmeal.[41] Five healthy pregnant pigtail macaques (*Macaca nemestrina*) received ZIKV (ZIKA 1–5) and three

animals served as controls (CTRL 1–3) (Fig. S1, Table S1). In early pregnancy, CTRL 3 had a subchorionic placental hemorrhage with vaginal bleeding (confirmed by ultrasound), which self-resolved; this animal was included in the study after her pregnancy stabilized and she had no bleeding for more than one month. Dual necropsy was performed earlier than planned for ZIKA 4 (~142 days) after an anesthetic reaction resulted in an unexpected death of the dam.

Definition of Fever in the Pigtail Macaque

The definition of a fever in a pigtail macaque is not standardized. A range of rectal temperatures has been reported in sedated rhesus and cynomolgus macaques (*Macaca mulatta and Macaca fascicularis*), which are close relatives to the pigtail that range from 36.6 – 40.1°C (average 38.8°C).[42] Individual variation is thought to relate to excitement prior to sedation and lowering of body temperature during sedation. The highest maternal rectal temperature recorded in the study was 38.6°C (101.5°F), which was not thought to represent a fever.

Mosquito Salivary Gland Extracts

The New Mexico State University IACUC approved the procedures associated with obtaining mosquito salivary glands (Permit Number: 2015-003). *Aedes aegypti* (Rockefeller strain) were maintained as described.[43] Larvae were reared at 26.5°C, 70% relative humidity, 16:8 hour light-dark cycle on a diet of cat food (Special Kitty, Walmart, USA); emerged adults were maintained on 20% sucrose *ad lib*. Salivary glands dissected on ice from adults after 3 days of age were placed in a drop of PBS and stored at −80°C. For homogenization, glands were aspirated >25 times using a syringe with 23-gauge needle and 10 μL PBS per gland; samples were centrifuged at 14,000 rpm for 10 min at 4°C and stored at −80°C.

Dengue Virus Antibody

A monoclonal antibody to a dengue virus (DENV) envelope dimer dependent epitope (EDE2 B7, IgG1 isotype) was synthetically generated by Lake Pharma from a published sequence, which is available upon request.

Ultrasound in Nonhuman Primates

Fetal dates were determined by measurement of the crown rump length in early pregnancy (~40–55 days gestation). Ultrasound was performed weekly starting with ZIKV or media inoculation for the duration of the study to confirm fetal viability, survey fetal brain structure, and perform standard fetal ultrasound biometric measures, which were compared with published standards in pigtail macaques.[44] A GE Vivid-i (GE Medical) machine was used for the first ultrasound and subsequent measurements were performed on the Philips HD11xe machine (Philips Healthcare). A curvilinear C9-4MHz transducer was used to image the fetus. At least three measurements of the head circumference, abdominal circumference, biparietal diameter and femur length were acquired and the average calculated. Additionally, at least three ventricular measurements in the dependent ventricle, transverse cerebellar diameter and placental thickness were acquired and average

measurement calculated. At least two cine clips were acquired through the head (axial and coronal orientation), chest and abdomen (axial and sagittal orientation). Doppler ultrasound of the middle cerebral artery was performed to evaluate the flow through the brain. Amniotic fluid index was calculated by measuring the fluid pockets in the four quadrants. Fetal biometry was compared to known standards for the pigtail macaque.[44] A board-certified radiologist (M.K.D.) with 13 years of experience in obstetric ultrasound reviewed the imaging. If a particular measurement or image was considered inadequate, this was excluded from the analysis.

Magnetic Resonance Imaging in Nonhuman Primates

Magnetic resonance imaging (MRI) was performed using a Philips Achieva 3T scanner. A six-channel human cardiac RF coil was used for the early studies and an eight-channel human knee coil for the later studies, once it was determined that pregnant animals near term could fit in the knee coil. Anesthesia was induced using 5–20 mg/kg ketamine and maintained using no higher than a 3% sevoflurane-oxygen mixture during the imaging. A three-plane localizer using a balanced FFE imaging sequence was used to determine fetal head position. A 2D single-shot, half-Fourier turbo spin echo multi-slice sequence (HASTE) was used to acquire T2-weighted images with the following parameters: TR/TE = 2200/160 ms, SENSE acceleration factor = 2, TSE factor = 100, along with fat suppression, and fold-over artifact suppression. Multiple contiguous 2D image stacks, with in-plane resolutions of 0.5×0.5 mm and thicknesses of 2 mm, were acquired along the axial, sagittal, and coronal axes of the fetal brain to facilitate the reconstruction of a 3D volume with isotropic spatial resolution. Each 2 mm thick plane orientation was repeated 6 times to provide high signal to noise in the final combined 3D reconstruction. MRI images were reviewed by a pediatric neuroradiologist (D.W.W.S.).

The first step to generate a single high resolution 3D T2W image volume for quantitative analysis of tissue brain volume and surface anatomy was to import all multi-slice T2-weighted image stacks with the SLIMMER slice motion correction tool[45] in Rview software (http://rview.colin-studholme.net, version 9.077.155BQT running under Ubuntu release 14). This step allowed for initial volume based alignment to correct for gross drift of the fetal head between slice stacks, and to define a standardize orientation of the fetal head anatomy. Between slice motion occurring due to maternal breathing and fetal head drift was estimated using slice intersection motion correction.[46] Differences in signal intensity arising from drift of the fetal head with respect to the imaging coils during scanning, and intensity variations due to spin history arising from motion between excitation and readout of each individual slice were corrected using slice intersection bias correction. Then, all slices were combined using an iterative deconvolution based super resolution 3D scattered data reconstruction technique, using robust Huber-norm outlier rejection of any residual within-slice motion artifacts.[47] The final de-convolved isotropic spatial sampling resolutions of each image were selected to match the in-plane resolution of each slice (0.5 mm).

As no age-specific atlas is available for this species over this gestational period, we first manually traced tissues in selected MRI's of the healthy reference fetuses so that we had a set of reference templates covering the full gestational age range of the study. This was

achieved using an initial approximate automated intensity based segmentation that was extensively edited using the Rview segmentation tool (http:rview.colin-studholme.net, version 9.077.155BQT running under Ubuntu release 14) to divide the tissues further into cortical and deep grey matter, white matter, cerebellum, sulcal cerebrospinal fluid and ventricular cerebrospinal fluid. These manually delineated reference images providing an example image of tissues at different gestational ages were then used as age-specific tissue templates for automated segmentation of each of the additional MRI scans of controls and ZIKV-infected fetuses. For each new scan the nearest age matched manually delineated template was used as a reference template for automated expectation maximization based segmentation.[48] Each automated segmentation was manually checked and edited to remove any residual cortical or sub-cortical tissue segmentation errors, and to correct labeling of abnormal CSF regions that were not present in the normal fetal template data. Regions of age-abnormal fluid representing abnormal posterior ventricular CSF regions and any surrounding disconnected regions of high T2-weighted signal were separately labeled as abnormal fluid volume. From these labeled images, we calculated the total supratentorial cortical grey matter, white matter and deep grey matter, the total cerebellum volume and the abnormal fluid volume in cubic centimeters.

Bacterial Cultures

Bacterial cultures were performed to exclude microbial infection. Amniotic fluid collected at necropsy was plated on Tryptic Soy Agar (TSA) plates and incubated for 48h at 37°C in 5% CO_2. Swabs of maternal and fetal meninges, lungs and chorioamniotic membranes were streaked on TSA plates and incubated for 48 hours at 37°C in 5% CO_2. No bacteria were cultured from any sample.

Serology for WNV, CHIKV, DENV and ZIKV in Nonhuman Primates

We used viral-specific ELISA assays for ZIKV, WNV, CHIKV, and DENV IgG to test ultraviolet-inactivated serum according to the manufacturer's (Xpress Biosystems) instructions. Diluted plasma samples were added to the wells of the ELISA plate coated with viral antigens and incubated at 37°C for 45 min. Wells were washed 5× and peroxidase conjugate was added to each well and incubated for 45 min at 37°C. Following incubation, the plate was washed 5 times followed by the addition of 2,2'-azino-bis (3-ethylbenzothiazoline-6-sulphonic acid)-peroxidase substrate to each well. The plate was incubated at room temperature for 30 min and the absorbance of the colorimetric reaction in each well was read within 15 min on a plate reader at 405 nm.

Neuropathology, Immunohistochemistry and Quantitative Analyses

The Seattle Childrens' Hospital Research Laboratory Service Core performed immunohistochemistry for glial fibrillary acidic protein (GFAP), Tbr2 and Ki67 on formalin-fixed paraffin-embedded sections of cerebral cortex or hippocampus from the ZIKV-exposed animals and controls. Immunostaining was performed with an automated immunostainer (Ventana) using the reagents and dilutions shown in Table S5. Appropriate peroxidase-conjugated secondary antibodies and diaminobenzidine-based reaction product were used to visualize sites of immunoreactivity. All sections were blinded for quantitative analyses. Coded-sections were imaged using an Olympus VS120 Slide Scanner. Temporal

cortical subventricular zone (SVZ) and hippocampal dentate gyrus subgranular zone (SGZ) regions were defined using anatomical and methylene blue counterstained cellular landmarks based on the available reference NIH Blueprint Nonhuman Primate Atlas (http://www.blueprintnhpatlas.org rhesus macaque neonate 0 months). The SGZ included both the cell-dense SGZ, and ~125um into the underlying polymorphic layer. Immunoreactive cells were automatically segmented using HSV (Hue, Saturation, and Value)-thresholding. All identified cells were manually checked to correct for multiplicity and the number of positive single cells was determined per area (mm^2) using Olympus VS-Desktop software. Blinded cell counts were independently de-coded and statistically analyzed (as below).

Cell Lines and Virus

Vero cells obtained from the World Health Organization and C6/36 *Aedes albopictus* cells (ATCC) were cultured in Dulbecco's modified Eagle's medium (DMEM/Cellgro) supplemented with 10% fetal bovine serum (FBS; Hyclone), 2 mM L-glutamine, 1 mM sodium pyruvate, 100 U/mL of penicillin, 100 ug/mL of streptomycin, and 1× non-essential amino acids (Sigma). The World Reference Center of Emerging Viruses and Arboviruses provided the ZIKV strain isolated in Cambodia (FSS13025, 2010, GenBank Accession Number: KU955593) and Dr. M. Diamond (Washington University) provided the ZIKV strain from Brazil (Fortaleza, 2015, GenBank Accession Number: KX811222.1). Working stocks were obtained by plaque-purifying virus amplified in either Vero (Cambodia strain) or C6/36 cells (Brazil strain). Virus was adsorbed to cells in DMEM supplemented to contain 1% FBS at 37°C for 2 h. The inoculum was removed and virus propagated in media supplemented to contain 5% FBS, 2 mM L-glutamine, 1 mM sodium pyruvate, 100 U/mL of penicillin, 100 ug/mL of streptomycin, 20 mM HEPES, and 1× non-essential amino acids (Sigma). Supernatants were collected and spun at 2,000 RPM at 4°C for 10 min, and frozen in aliquots at −80°C. All cell lines used lacked mycoplasma.

Measurement of ZIKV RNA Load

Viral RNA load was assessed in tissues from the dam, fetus, and placenta using a ZIKV-specific RT-qPCR assay. Fetal and maternal organs were immersed in RNA-later immediately upon harvest and were then weighed and homogenized in RLT solution (Qiagen) using a bead-beater apparatus (Precellys). RNA was extracted from tissues using the RNeasy kit (Qiagen) and from sera using the ZR Viral RNA extraction kit (Zymo Research). From tissues, 400 ng of total RNA was used to generate cDNA using the iScript select cDNA synthesis kit (Bio-Rad) according to manufacturer's protocols for gene-specific primers. Viral RNA was quantified using the Taqman Universal Master Mix (Applied Biosystems) and an Applied Biosystems 7300 RT-PCR machine with primers that correspond to residues conserved in both the FSS13025 and Brazil Fortaleza genome (GenBank numbers KU955593.10, KX811222.1).[49] To adhere to stringent guidelines, Ct (cycle threshold) values >38 were deemed as not reliably detected and were not reported. Copy number sensitivity, as determined using a standard curve from diluted known quantities of ZIKV genome, was 25 copies/qPCR reaction.

ZIKV Isolation from Maternal Plasma

Confluent T75 flasks of C6/36 cells were incubated with 300 μL of dam plasma from CTRL 2, ZIKA 3, ZIKA 4, and ZIKA 5 in 2 stages; first, cells and plasma were incubated with 6.5 mL complete DMEM (cDMEM) for 2 hours at 28°C, and then, an additional 4 mL of cDMEM was added to each flask and incubated at 28°C for 2 days. Two days post-inoculation (dpi), growth media was replaced and cells were incubated for a further 7 days prior to harvest of culture fluid; at this time (9 dpi), culture fluid was harvested and centrifuged at $1,260 \times g$ for 10 min (4°C) to clear cell debris. Aliquots were stored at −80°C.

Immunofluorescence Detection of ZIKV in Vero cells

Vero cells seeded onto coverslips were inoculated with 150 μL of 9 dpi culture fluid derived from ZIKV infected nonhuman primate tissues and incubated at 37°C for 2 hrs with gentle rocking. Subsequently, media was replaced and infected cells were incubated for 22 hrs to allow virus growth, and then fixed for 30 min with 4% (w/v) paraformaldehyde in TBS. Fixed cells were washed with TBS and permeabilized for 10 min at −20°C with methanol. Cells were blocked with 5% (v/v) normal goat serum in TBS (NGS/TBS), and were stained with ZV-13 mouse monoclonal antibody reactive to ZIKV E protein (provided by Dr. M. Diamond, Washington University) in NGS/TBS.[50] Cells were subsequently incubated with goat anti-mouse IgG-Alexafluor 488 conjugate (cat# A-11029, Thermo Fisher Scientific, MA) in NGS/TBS, nuclei were counterstained with DAPI (4',6-Diamidino-2-Phenylindole, Dihydrochloride, cat# D1306, Thermo Fisher Scientific), and mounted on slides for analysis. Confocal immunofluorescence images were acquired using a Nikon Eclipse Ti microscope and analyzed using NIS-Elements imaging system software (version 4.51) (Nikon Instruments).

Immunofluorescence Detection of Tbr2, Sox2, and Dcx in Dentate Gyrus of the Fetal Hippocampus

Blinded and coded FFPE 5 μm sections were deparaffinized, and antigen retrieved by incubating slides in 10mM sodium citrate, pH 6.0, at 95° C in a water bath for 35 min, cooled to room temp, and transferred to PBT (1× phosphate-buffered saline (PBS) with 0.3% Triton X-100). Sections were blocked (PBT with 5% donkey serum and 5% BSA) for 1 hour, and incubated with Sox2, Tbr2, and Dcx primary antibodies overnight at room temp. Sections were washed 3× with PBT, species-specific ALEXA 488/568/647 fluorescent secondary antibodies were applied (1:500) and incubated for 2h at room temp, washed and counterstained with DAPI, and mounted in Fluoromount-G. Confocal microscopic (20×) image volumes were acquired using a Zeiss 710 34-Quasar LSCM from the same 4 representative regions across the length of each dentate gyrus. Blinded and coded image volumes were visualized and analyzed using Imaris (Bitplane). Snapshots of overlaid and individual image volumes were exported, and assembled using Adobe Photoshop and Illustrator.

Flow Cytometry on Placental Tissues, Maternal Blood and Fetal Brain

To generate single-cell suspensions, chorioamniotic membranes were washed twice in sterile PBS, weighed, and re-suspended in digestion buffer (10 mL/g tissue; 20 mM HEPES, 30

mM NaHCO3, 10 mg/mL BSA, 150 μg/mL DNase, 1 mg/mL bovine testes hyaluronidase, 200 U/mL collagenase 1a, 100 U/mL penicillin, and 100 μg/mL streptomycin). The membranes were minced for 2 min and incubated at 37°C at 300 rpm for 1 hr. Tissues were progressively filtered through a 280μm metal sieve and 100, 70 and 40 μm nylon screens, respectively. Single cells were pelleted at $300 \times g$ for 5 min and re-suspended in RPMI supplemented with 10% heat inactivated fetal bovine serum, 100 U/mL penicillin, 100μg/mL streptomycin and placed on ice. Erythrocyte lysis was performed on placental and maternal blood single-cell suspensions by re-suspending cells in erythrocyte lysing solution (lysis solution volume equal to 10 volume of cell pellet; 0.15 nM NH4Cl, 1 mM NaHCO3) followed by 15 min incubation at room temperature. This process was repeated 3–5 times, until erythrocytes were visibly absent. To generate single-cell suspensions of white matter and hippocampal tissues, each sample was filtered through a 280 μm metal sieve, pelleted at $300 \times g$ for 5 min, washed once in sterile PBS, and re-suspended in FACS buffer (1mM EDTA, 25mM HEPES, and 0.1% BSA (w/v) in PBS). Single-cell suspensions from all tissues were counted using the TC20 cell counter (BioRad), and diluted to approximately 10^7 cells/mL in FACS buffer. Cell suspensions from the fetal hippocampus were stored in formalin or 3.7% paraformaldehyde (1:2) at 4°C or −80°C, respectively, until samples from each animal were collected.[51]

Extracellular staining

Prior to staining, cells from all tissues were pre-treated with Fc block (1:200, BD Biosciences) for 15 min. Cell suspensions from white matter tissue were stained with anti-CD56 V450 for 35 min (Table S5); and cells from the placental membranes and maternal blood were stained with anti-CD3-FITC, anti-CD8-PerCP/Cy5.5, and anti-CD16-PE/Cy7 for 35 min (Table S5). Cells were washed twice in FACS buffer to remove excess antibody.

Intracellular staining

Cells from white matter tissue were treated with the Foxp3/Transcription Factor Staining Buffer Set (eBioscience) per manufacturer's instructions. Cells were stained with anti-GFAP-APC for 35 min (Table S5), and then washed twice in permeabilization buffer (eBioscience) and re-suspended in FACS buffer. At the time of analysis, hippocampal cells were washed twice with FACS buffer to remove residual fixative and permeabilized in 1× PBS, 0.1% Triton X-100 (Sigma-Aldrich, MO), 1% BSA for 10 min on ice. Following permeabilization, cells were split into equal volumes and washed twice in FACS buffer. Hippocampal cells were treated with anti-Tbr2-PE for 35 min (Table S5), and then washed twice in FACS buffer to remove excess antibody.

Analysis

All stained cells were analyzed using an LSRII flow cytometer (BD Biosciences). Unstained and single color compensation beads (BD Biosciences) were included for compensation. Cell surface and intracellular markers were analyzed using FlowJo software version 10.1 (FlowJo).

Flow Cytometry on Blood for Antibody-Dependent Enhancement Experiments

Peripheral blood from two healthy, flavivirus-naïve adult pigtail macaques (CTRL I and J, Table S1) were used to obtain peripheral blood mononuclear cells (PBMC), which were enriched using density gradient centrifugation with Ficoll-Paque PLUS (GE Healthcare). Erythrocytes were lysed with ACK Lysis buffer (Gibco). Total PBMC were resuspended in serum-free infection media (RPMI 1640 media plus 0.1 mM nonessential amino acids, 100 U/ml penicillin, 100 mg/ml streptomycin, 2 mM GlutaMAX, 10 mM HEPES (Cellgro) and 2-mercaptoethanol). The EDE2 B7 monoclonal antibody was synthesized by Lake Pharma (Belmont, CA). ZIKV PRVABC59 was originally obtained from the Centers of Disease Control and Prevention (Atlanta, GA), and 800 μl of ZIKV-infected C6/36 cell culture supernatant was used per well in this assay. Uninfected C6/36 cell culture supernatant ('spent media', 800 μl) was used for wells not treated with ZIKV. Treatment conditions included: 1) no antibody and no virus, 2) no antibody plus ZIKV, 3) 5 μg/ml isotype antibody control (BioXcell) plus ZIKV, or 4) 1 μg/ml EDE2 B7 antibody plus ZIKV. All conditions were assayed in duplicate on 12-well plates (Corning). Virus and antibodies were first added to appropriate wells, mixed well, and incubated at 37°C and 5% CO_2 for 1 hour, after which 2×10^6 PBMC were added per well. After 2 hours of incubation, 1 ml of 10% inactivated FBS (Gibco) infection media was added to each well, and cultures were collected after 20 hours. Adherent cells were treated with 5 mM cold EDTA at 4°C for 30 minutes to assist with cell detachment and were gently removed using soft rubber-tipped scrapers (Falcon). Detached cell fractions were combined with suspension cultures, washed with Flow Cytometry Staining Buffer (eBioscience/Thermo Fisher Scientific), and stained with antibodies targeting surface markers CD14 (clone M5E2; BD Biosciences) and HLA-DR (clone G46-6; BD Biosciences), in the presence of Fixable Live/Dead Discriminator (Invitrogen). Cells were fixed and permeabilized using Intracellular Fixation and Permeabilization Buffers (eBioscience/Thermo Fisher Scientific) according to manufacturer's instructions. Intracellular staining with 4G2 antibody conjugated to AlexaFluor 488 (Molecular Probes) was used to detect ZIKV antigen. Cells were fixed in 1% formalin, transferred to staining buffer, and acquired on an LSRII cytometer (BD). Cells were first gated to exclude debris, omit doublet events, and remove dead cells from analysis. CD14+HLA-DR+ double positive events ('monocytes') were analyzed for the presence of ZIKV antigen. Cytometric data were analyzed using FlowJo X software (TreeStar).

Statistical Analysis

An unpaired two-tailed t-test with unequal variances (Welch) was used for all statistical analyses and p value <0.05 was considered significant. Statistical analysis was performed using Graph Pad Prism (version 6.0, GraphPad Software, USA, www.graphpad.com) and Stata (version 14.2, StataCorp, TX). The fetal brain volume ratio analysis excluded ZIKA 4, because final MRI data was obtained ~30 days earlier in this case than for all other cases and controls.

Data Availability

No large datasets were generated or analyzed during the current study. All data analyzed in this study are included in this published article (and its supplementary information files).

Supplementary Material

Refer to Web version on PubMed Central for supplementary material.

Acknowledgments

References

1. van den Pol AN, Mao G, Yang Y, Ornaghi S, Davis JN. Zika virus targeting in the developing brain. J Neurosci. 2017

2. Moore CA, et al. Characterizing the Pattern of Anomalies in Congenital Zika Syndrome for Pediatric Clinicians. JAMA Pediatr. 2016

3. Maurice J. The Zika virus public health emergency: 6 months on. Lancet. 2016; 388:449–450. [PubMed: 27507747]

4. Franca GVA, et al. Congenital Zika virus syndrome in Brazil: a case series of the first 1501 livebirths with complete investigation. Lancet. 2016; 388:891–897. [PubMed: 27372398]

5. Mlakar J, et al. Zika Virus Associated with Microcephaly. N Engl J Med. 2016

6. Driggers RW, et al. Zika Virus Infection with Prolonged Maternal Viremia and Fetal Brain Abnormalities. N Engl J Med. 2016

7. Moura da Silva AA, et al. Early Growth and Neurologic Outcomes of Infants with Probable Congenital Zika Virus Syndrome. Emerg Infect Dis. 2016; 22:1953–1956. [PubMed: 27767931]

8. Del Campo M, et al. The phenotypic spectrum of congenital Zika syndrome. Am J Med Genet A. 2017; 173:841–857. [PubMed: 28328129]

9. Richner JM, et al. Modified mRNA Vaccines Protect against Zika Virus Infection. Cell. 2017; 168:1114–1125 e1110. [PubMed: 28222903]

10. Betancourt D, de Queiroz NM, Xia T, Ahn J, Barber GN. Cutting Edge: Innate Immune Augmenting Vesicular Stomatitis Virus Expressing Zika Virus Proteins Confers Protective Immunity. J Immunol. 2017

11. Chahal JS, et al. An RNA nanoparticle vaccine against Zika virus elicits antibody and CD8+ T cell responses in a mouse model. Sci Rep. 2017; 7:252. [PubMed: 28325910]

12. Sumathy K, et al. Protective efficacy of Zika vaccine in AG129 mouse model. Sci Rep. 2017; 7:46375. [PubMed: 28401907]

13. Shan C, et al. A live-attenuated Zika virus vaccine candidate induces sterilizing immunity in mouse models. Nat Med. 2017

14. Yang Y, et al. A cDNA Clone-Launched Platform for High-Yield Production of Inactivated Zika Vaccine. EBioMedicine. 2017; 17:145–156. [PubMed: 28196656]

15. Sapparapu G, et al. Neutralizing human antibodies prevent Zika virus replication and fetal disease in mice. Nature. 2016; 540:443–447. [PubMed: 27819683]

16. Ireton RC, Gale M Jr. RIG-I like receptors in antiviral immunity and therapeutic applications. Viruses. 2011; 3:906–919. [PubMed: 21994761]

17. Adams Waldorf KM, et al. Fetal brain lesions after subcutaneous inoculation of Zika virus in a pregnant nonhuman primate. Nat Med. 2016; 22:1256–1259. [PubMed: 27618651]

18. Styer LM, et al. Mosquito saliva causes enhancement of West Nile virus infection in mice. J Virol. 2011; 85:1517–1527. [PubMed: 21147918]

19. Conway MJ, et al. Mosquito saliva serine protease enhances dissemination of dengue virus into the mammalian host. J Virol. 2014; 88:164–175. [PubMed: 24131723]

20. Swanstrom JA, et al. Dengue Virus Envelope Dimer Epitope Monoclonal Antibodies Isolated from Dengue Patients Are Protective against Zika Virus. MBio. 2016; 7

21. Dejnirattisai W, et al. Dengue virus sero-cross-reactivity drives antibody-dependent enhancement of infection with zika virus. Nat Immunol. 2016

22. Paul LM, et al. Dengue virus antibodies enhance Zika virus infection. Clin Transl Immunology. 2016; 5:e117.

23. Lin MY, et al. Zika Virus Infects Intermediate Progenitor Cells and Post-mitotic Committed Neurons in Human Fetal Brain Tissues. Sci Rep. 2017; 7:14883. [PubMed: 29093521]

24. Onorati M, et al. Zika Virus Disrupts Phospho-TBK1 Localization and Mitosis in Human Neuroepithelial Stem Cells and Radial Glia. Cell Rep. 2016; 16:2576–2592. [PubMed: 27568284]

25. Smart IH, Dehay C, Giroud P, Berland M, Kennedy H. Unique morphological features of the proliferative zones and postmitotic compartments of the neural epithelium giving rise to striate and extrastriate cortex in the monkey. Cereb Cortex. 2002; 12:37–53. [PubMed: 11734531]

26. Bakken TE, et al. A comprehensive transcriptional map of primate brain development. Nature. 2016; 535:367–375. [PubMed: 27409810]

27. Miller JA, et al. Conserved molecular signatures of neurogenesis in the hippocampal subgranular zone of rodents and primates. Development. 2013; 140:4633–4644. [PubMed: 24154525]

28. Alvarez-Buylla A, Lim DA. For the long run: maintaining germinal niches in the adult brain. Neuron. 2004; 41:683–686. [PubMed: 15003168]

29. Goncalves JT, Schafer ST, Gage FH. Adult Neurogenesis in the Hippocampus: From Stem Cells to Behavior. Cell. 2016; 167:897–914. [PubMed: 27814520]

30. McGrath EL, et al. Differential Responses of Human Fetal Brain Neural Stem Cells to Zika Virus Infection. Stem Cell Reports. 2017; 8:715–727. [PubMed: 28216147]

31. Hodge RD, et al. Tbr2 expression in Cajal-Retzius cells and intermediate neuronal progenitors is required for morphogenesis of the dentate gyrus. J Neurosci. 2013; 33:4165–4180. [PubMed: 23447624]

32. Hodge RD, et al. Tbr2 is essential for hippocampal lineage progression from neural stem cells to intermediate progenitors and neurons. J Neurosci. 2012; 32:6275–6287. [PubMed: 22553033]

33. Spalding KL, et al. Dynamics of hippocampal neurogenesis in adult humans. Cell. 2013; 153:1219–1227. [PubMed: 23746839]

34. Mu Y, Gage FH. Adult hippocampal neurogenesis and its role in Alzheimer's disease. Mol Neurodegener. 2011; 6:85. [PubMed: 22192775]

35. Duan X, et al. Disrupted-In-Schizophrenia 1 regulates integration of newly generated neurons in the adult brain. Cell. 2007; 130:1146–1158. [PubMed: 17825401]

36. Jacobs BL, van Praag H, Gage FH. Adult brain neurogenesis and psychiatry: a novel theory of depression. Mol Psychiatry. 2000; 5:262–269. [PubMed: 10889528]

37. Li H, et al. Zika Virus Infects Neural Progenitors in the Adult Mouse Brain and Alters Proliferation. Cell Stem Cell. 2016; 19:593–598. [PubMed: 27545505]

38. Rice D, Barone S Jr. Critical periods of vulnerability for the developing nervous system: evidence from humans and animal models. Environ Health Perspect. 2000; 108(Suppl 3):511–533. [PubMed: 10852851]

39. McCracken MK, et al. Impact of prior flavivirus immunity on Zika virus infection in rhesus macaques. PLoS Pathog. 2017; 13:e1006487. [PubMed: 28771605]

40. Katzelnick LC, et al. Antibody-dependent enhancement of severe dengue disease in humans. Science. 2017

41. Styer LM, et al. Mosquitoes inoculate high doses of West Nile virus as they probe and feed on live hosts. PLoS Pathog. 2007; 3:1262–1270. [PubMed: 17941708]

42. Woods SE, Marini RP, Patterson MM. Noninvasive temporal artery thermometry as an alternative to rectal thermometry in research macaques (Macaca spp.). J Am Assoc Lab Anim Sci. 2013; 52:295–300. [PubMed: 23849413]

43. Price DP, et al. The fat body transcriptomes of the yellow fever mosquito Aedes aegypti, pre- and post- blood meal. PLoS One. 2011; 6:e22573. [PubMed: 21818341]

44. Conrad S, Ha J, Lohr C, Sackett G. Ultrasound measurement of fetal growthin Macaca nemestrina. Am J Primatol. 1995; 36:15–35.

45. Kim K, et al. Intersection based motion correction of multislice MRI for 3-D in utero fetal brain image formation. IEEE Trans Med Imaging. 2010; 29:146–158. [PubMed: 19744911]

46. Kim K, et al. Bias field inconsistency correction of motion-scattered multislice MRI for improved 3D image reconstruction. IEEE Trans Med Imaging. 2011; 30:1704–1712. [PubMed: 21511561]

47. Fogtmann M, et al. A unified approach to diffusion direction sensitive slice registration and 3-D DTI reconstruction from moving fetal brain anatomy. IEEE Trans Med Imaging. 2014; 33:272–289. [PubMed: 24108711]

48. Habas PA, et al. A spatiotemporal atlas of MR intensity, tissue probability and shape of the fetal brain with application to segmentation. Neuroimage. 2010; 53:460–470. [PubMed: 20600970]

49. Lanciotti RS, et al. Genetic and serologic properties of Zika virus associated with an epidemic, Yap State, Micronesia, 2007. Emerg Infect Dis. 2008; 14:1232–1239. [PubMed: 18680646]

50. Zhao H, et al. Structural Basis of Zika Virus-Specific Antibody Protection. Cell. 2016; 166:1016–1027. [PubMed: 27475895]

51. Thomsen ER, et al. Fixed single-cell transcriptomic characterization of human radial glial diversity. Nat Methods. 2016; 13:87–93. [PubMed: 26524239]
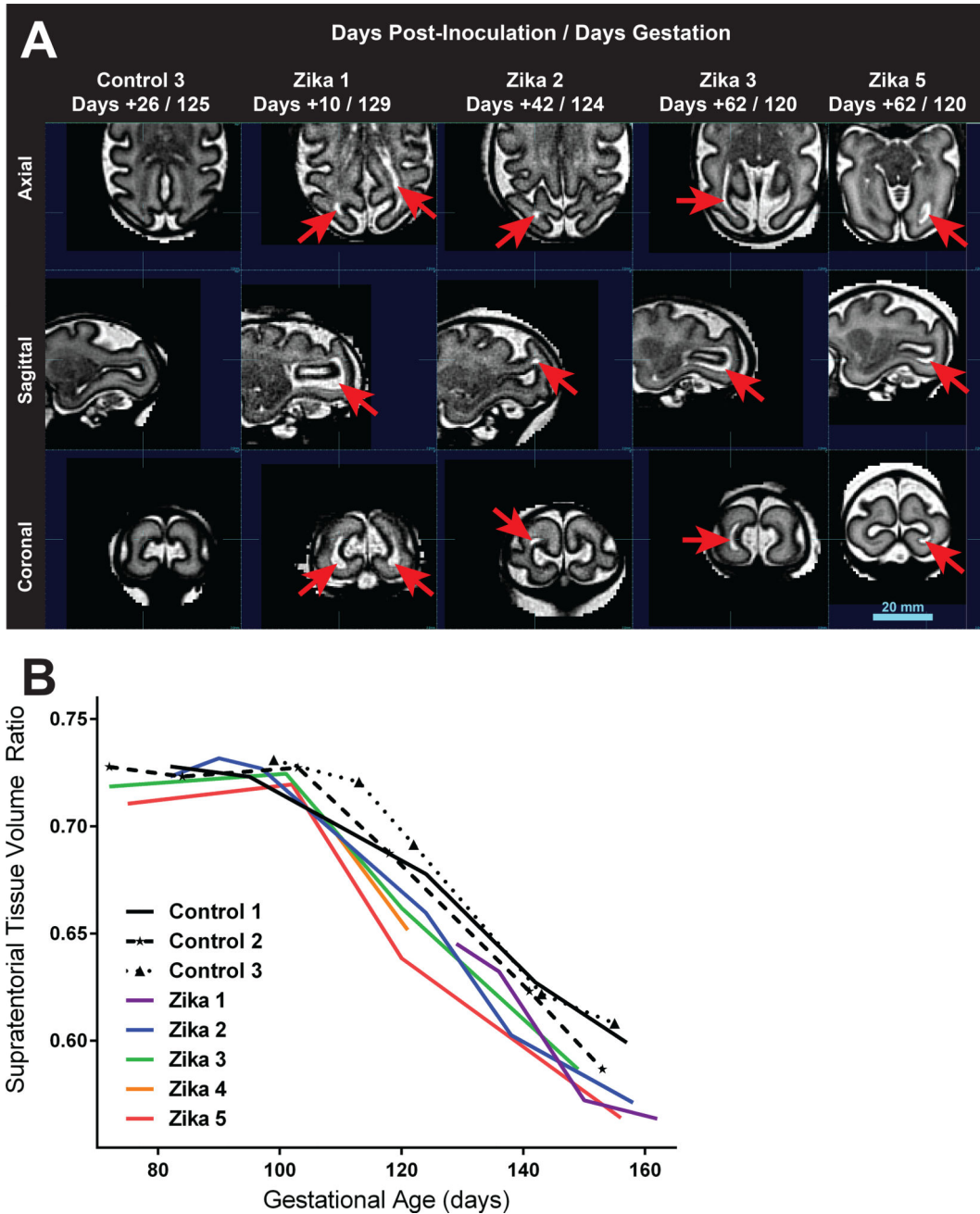
Figure 1.

Fetal Brain MRI Imaging and Volume Analysis. Serial fetal brain MRI images (HASTE) from pigtail macaques inoculated with ZIKV and control media were analyzed for differences in structure and volume. Four of five ZIKV animals demonstrated periventricular-subcortical T2-hyperintense foci in the posterior brain between 120–129 days, which were absent in control fetuses at the same developmental age (A). Images were segmented to obtain specific brain volumes of each region (e.g. white matter, cortical gray matter, Fig. S13). The plot (B) demonstrates the change in the supratentorial (fetal brain) tissue volume ratio in the latter half of pregnancy; this ratio estimates the contribution of
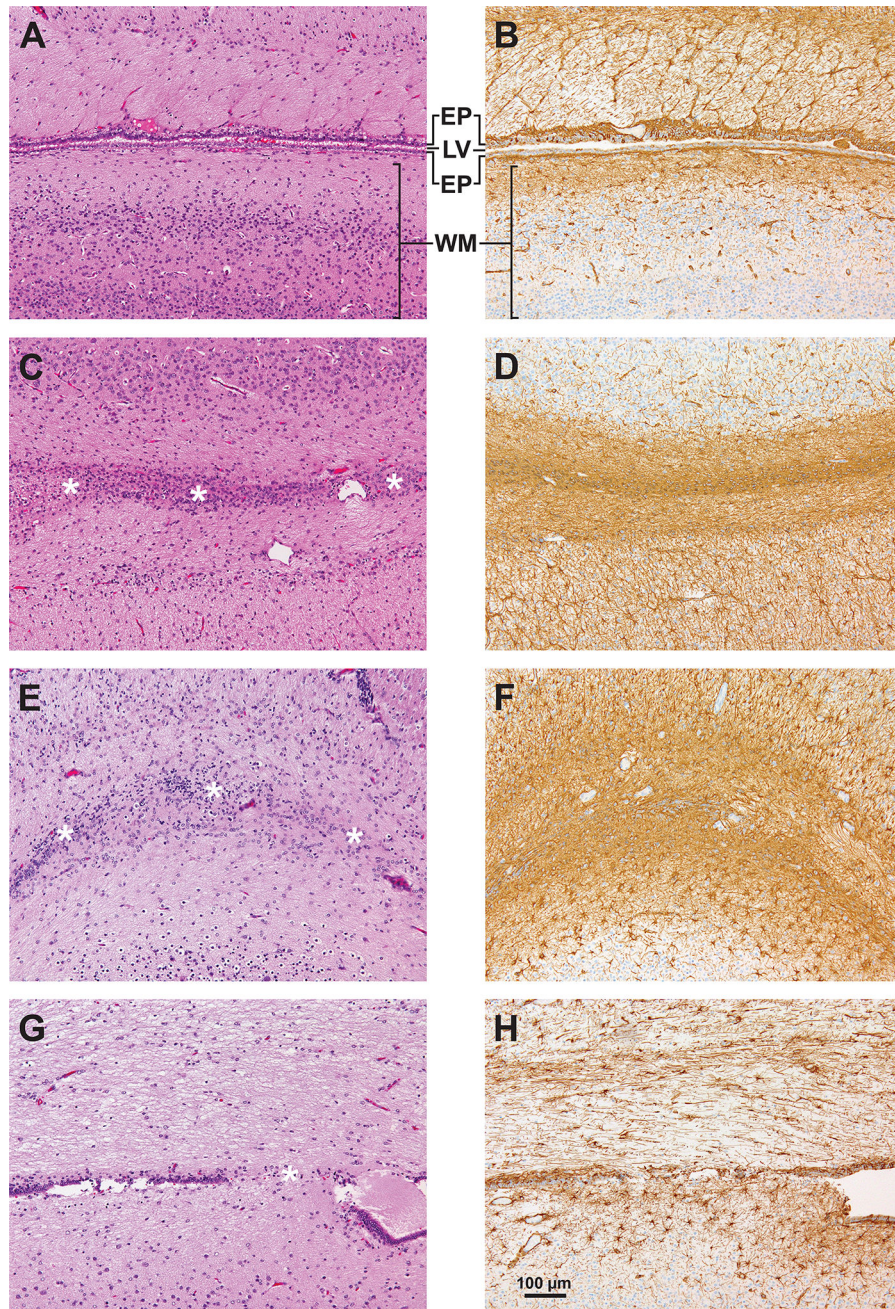
non-cortical tissues (excluding cortical plate) to the overall volume of the brain (excluding cerebellum).

Figure 2.
Neuropathology of the Fetal Brain Demonstrating ZIKV-Associated Ependymal Fusion and Periventricular Gliosis. Microscopic images of hematoxylin and eosin stained sections of the lateral ventricle (LV) with ependymal epithelium (EP) are shown for a control (A) and ZIKA 1, 2 and 4 (C, E, G, respectively). Immunostaining for GFAP is also shown in the same control (B) and ZIKV-infected animals (D, F, H) in an adjacent section. Asterisks indicate zones of ependymal fusion. GFAP-immunostaining demonstrates periventricular gliosis (brown staining) in regions surrounding ependymal fusion. WM, white matter.

This is an Adobe® Illustrator® File that was saved without PDF Content.
To Place or open this file in other applications, it should be re-saved from Adobe Illustrator with the "Create PDF Compatible File" option turned on. This option is in the Illustrator Native Format Options dialog box, which appears when saving an Adobe Illustrator file using the Save As command.

This is an Adobe® Illustrator® File that was saved without PDF Content.
To Place or open this file in other applications, it should be re-saved from Adobe Illustrator with the "Create PDF Compatible File" option turned on. This option is in the Illustrator Native Format Options dialog box, which appears when saving an Adobe Illustrator file using the Save As command.

This is an Adobe® Illustrator® File that was saved without PDF Content.
To Place or open this file in other applications, it should be re-saved from Adobe Illustrator with the "Create PDF Compatible File" option turned on. This option is in the Illustrator Native Format Options dialog box, which appears when saving an Adobe Illustrator file using the Save As command.

This is an Adobe® Illustrator® File that was saved without PDF Content.
To Place or open this file in other applications, it should be re-saved from Adobe Illustrator with the "Create PDF Compatible File" option turned on. This option is in the Illustrator Native Format Options dialog box, which appears when saving an Adobe Illustrator file using the Save As command.

This is an Adobe® Illustrator® File that was saved without PDF Content.
To Place or open this file in other applications, it should be re-saved from Adobe Illustrator with the "Create PDF Compatible File" option turned on. This option is in the Illustrator Native Format Options dialog box, which appears when saving an Adobe Illustrator file using the Save As command.

This is an Adobe® Illustrator® File that was saved without PDF Content.
To Place or open this file in other applications, it should be re-saved from Adobe Illustrator with the "Create PDF Compatible File" option turned on. This option is in the Illustrator Native Format Options dialog box, which appears when saving an Adobe Illustrator file using the Save As command.

This is an Adobe® Illustrator® File that was saved without PDF Content.
To Place or open this file in other applications, it should be re-saved from Adobe Illustrator with the "Create PDF Compatible File" option turned on. This option is in the Illustrator Native Format Options dialog box, which appears when saving an Adobe Illustrator file using the Save As command.

This is an Adobe® Illustrator® File that was saved without PDF Content.
To Place or open this file in other applications, it should be re-saved from Adobe Illustrator with the "Create PDF Compatible File" option turned on. This option is in the Illustrator Native Format Options dialog box, which appears when saving an Adobe Illustrator file using the Save As command.

Figure 3.
Reduced NSC proliferation in late fetal neurogenic zones. A schematic of the fetal temporal cortical subventricular zone (SVZ) and hippocampus is shown for a rhesus macaque neonate (0 months) with a Nissl stained section (A) and diagrams to indicate locations of proliferating Ki67+ NSCs (pink dots and pink regions) in neurogenic niches of the tissue (B) and specific regions of the SVZ and hippocampus (C). Ki67+ cells in the dentate gyrus and the SVZ, key regions of neurogenesis, are shown for a control (row D) and ZIKA fetuses (E–G), with higher power views of the dentate gyrus (blue box) and SVZ regions (pink box) to the right. (H) Quantitation of Ki67+ cells reveals a significant decrease in proliferation in

the SVZ of ZIKV-infected animals compared to SGZ and controls. The dentate gyrus zones include the molecular layer (ML), granule zone (GZ), subgranular zone (SGZ), polymorphic layer (PM), and the hilus (H). Adjacent areas to the dentate include the cornu ammonis (CA) and subiculum. The lateral ventricle (LV) is lined by ependymal epithelium (E) with an underlying SVZ. Data shown as mean ± standard deviation of $Ki67^+$ cell counts per mm^2 (*$p<0.05$). The schematic (A) is based on the NIH Blueprint Nonhuman Primate Atlas (http://www.blueprintnhpatlas.org).

This is an Adobe® Illustrator® File that was saved without PDF Content.
To Place or open this file in other applications, it should be re-saved from Adobe Illustrator with the "Create PDF Compatible File" option turned on. This option is in the Illustrator Native Format Options dialog box, which appears when saving an Adobe Illustrator file using the Save As command.

This is an Adobe® Illustrator® File that was saved without PDF Content.
To Place or open this file in other applications, it should be re-saved from Adobe Illustrator with the "Create PDF Compatible File" option turned on. This option is in the Illustrator Native Format Options dialog box, which appears when saving an Adobe Illustrator file using the Save As command.

This is an Adobe® Illustrator® File that was saved without PDF Content.
To Place or open this file in other applications, it should be re-saved from Adobe Illustrator with the "Create PDF Compatible File" option turned on. This option is in the Illustrator Native Format Options dialog box, which appears when saving an Adobe Illustrator file using the Save As command.

This is an Adobe® Illustrator® File that was saved without PDF Content.
To Place or open this file in other applications, it should be re-saved from Adobe Illustrator with the "Create PDF Compatible File" option turned on. This option is in the Illustrator Native Format Options dialog box, which appears when saving an Adobe Illustrator file using the Save As command.

This is an Adobe® Illustrator® File that was saved without PDF Content.
To Place or open this file in other applications, it should be re-saved from Adobe Illustrator with the "Create PDF Compatible File" option turned on. This option is in the Illustrator Native Format Options dialog box, which appears when saving an Adobe Illustrator file using the Save As command.

This is an Adobe® Illustrator® File that was saved without PDF Content.
To Place or open this file in other applications, it should be re-saved from Adobe Illustrator with the "Create PDF Compatible File" option turned on. This option is in the Illustrator Native Format Options dialog box, which appears when saving an Adobe Illustrator file using the Save As command.

This is an Adobe® Illustrator® File that was saved without PDF Content.
To Place or open this file in other applications, it should be re-saved from Adobe Illustrator with the "Create PDF Compatible File" option turned on. This option is in the Illustrator Native Format Options dialog box, which appears when saving an Adobe Illustrator file using the Save As command.

This is an Adobe® Illustrator® File that was saved without PDF Content.
To Place or open this file in other applications, it should be re-saved from Adobe Illustrator with the "Create PDF Compatible File" option turned on. This option is in the Illustrator Native Format Options dialog box, which appears when saving an Adobe Illustrator file using the Save As command.

Figure 4.
Attenuated neurogenesis in late fetal neurogenic zones accompanied by granule neuron dysmorphia in the dentate gyrus after maternal ZIKV infection. (A–C) Adjacent sections were labeled for Sox2+ NSCs (left sections) and Tbr2+ IPs (right sections) by immunohistochemistry (brown, Tbr2 is also known as Eomes) and quantified by image analysis (D, E). Fetal Sox2+ NSCs were significantly reduced in the SVZ and disorganized in the subgranular zone (SGZ) with congenital ZIKV exposure. In the SGZ, there was a significant and marked reduction in Tbr2+ IPs in ZIKA fetuses compared to controls. Asterisks indicate disordered NSC in the SGZ neurogenic niche. Arrows indicate a loss of

continuity in the granule zone. (F–H) Confocal microscopy to identify NSCs (Sox2+, red), IPs (Tbr2+, green) and immature granule neurons (Dcx, doublecortin, white; Dapi nuclei, blue) in adjacent sections revealed disordered NSCs in the SGZ niche, loss of neurogenic output (Tbr2+ IPs), and dysmorphic granule neurons with congenital ZIKV exposure. Data shown as mean ± standard deviation of either Sox2$^+$ or Tbr2$^+$ cell counts per mm^2 (**$p < 0.01$).